

Article

Effect of Neutron Flux on an Irradiation-Induced Microstructure and Hardening of Reactor Pressure Vessel Steels

Andreas Ulbricht ^{1,*}, Mercedes Hernández-Mayoral ² , Elvira Oñorbe ² , Auriane Etienne ³, Bertrand Radiguet ³, Eric Hirschmann ¹ , Andreas Wagner ¹, Hieronymus Hein ⁴ and Frank Bergner ¹ 

¹ Helmholtz-Zentrum Dresden-Rossendorf, Bautzner Landstraße 400, D-01328 Dresden, Germany; e.hirschmann@hzdr.de (E.H.); a.wagner@hzdr.de (A.W.); f.bergner@hzdr.de (F.B.)

² Centro de Investigaciones Energéticas, Medioambientales y Tecnológicas (CIEMAT), Avda. Complutense 40, 28040 Madrid, Spain; m.mayoral@ciemat.es (M.H.-M.); elvira.onorbe@ciemat.es (E.O.)

³ Groupe de Physique des Matériaux, Université et INSA de Rouen, UMR CNRS 6634, B.P.12, CEDEX, 76801 Saint-Etienne du Rouvray, France; auriane.etienne@univ-rouen.fr (A.E.); bertrand.radiguet@univ-rouen.fr (B.R.)

⁴ Framatome GmbH, Erlangen, Paul-Gossen-Str. 100, D-91052 Erlangen, Germany; hieronymus.hein@framatome.com

* Correspondence: a.ulbricht@hzdr.de

Abstract: The existing knowledge about the effect of neutron irradiation on the mechanical properties of reactor pressure vessel steels under reactor service conditions relies to a large extent on accelerated irradiations realized by exposing steel samples to a higher neutron flux. A deep understanding of flux effects is, therefore, vital for gaining service-relevant insight into the mechanical property degradation. The existing studies on flux effects often suffer from incomplete descriptions of the irradiation-induced microstructure. Our study aims to give a detailed picture of irradiation-induced nanostructures by applying complementary methods using atom probe tomography, positron annihilation, small-angle neutron scattering and transmission electron microscopy. The characteristics of the irradiation-induced nanostructures and the dominant factors responsible for the observed increase of Vickers hardness are identified. Microstructural changes due to high flux conditions are smaller nm-sized solute atom clusters with almost the same volume fraction and a higher concentration of vacancies and sub-nm vacancy clusters compared to low flux conditions. The results rationalize why pronounced flux effects on the nanostructures, in particular on solute atom clusters, only give rise to small or moderate flux effects on hardening.

Keywords: reactor pressure vessel steel; neutron irradiation; flux effect; microstructure; atom probe tomography; positron annihilation spectroscopy; small-angle neutron scattering; TEM



Citation: Ulbricht, A.; Hernández-Mayoral, M.; Oñorbe, E.; Etienne, A.; Radiguet, B.; Hirschmann, E.; Wagner, A.; Hein, H.; Bergner, F. Effect of Neutron Flux on an Irradiation-Induced Microstructure and Hardening of Reactor Pressure Vessel Steels. *Metals* **2022**, *12*, 369. <https://doi.org/10.3390/met12030369>

Academic Editors: Ferenc Gillemot and Giovanni Principi

Received: 18 January 2022

Accepted: 19 February 2022

Published: 22 February 2022

Publisher's Note: MDPI stays neutral with regard to jurisdictional claims in published maps and institutional affiliations.



Copyright: © 2022 by the authors. Licensee MDPI, Basel, Switzerland. This article is an open access article distributed under the terms and conditions of the Creative Commons Attribution (CC BY) license (<https://creativecommons.org/licenses/by/4.0/>).

1. Introduction

The irradiation of reactor pressure vessel (RPV) steels with energetic neutrons gives rise to the formation of several kinds of nanostructures, including vacancy clusters, dislocation loops, Cu-rich clusters and Mn-Ni-Si-rich solute atom clusters [1–5]. These nanostructures impede the dislocation slip resulting in a degradation of the mechanical properties, i.e., irradiation hardening and embrittlement. It is important to note that embrittlement may also be partly due to radiation-induced segregation to grain boundaries, resulting in intergranular fracture [6–9]. This so-called non-hardening embrittlement can also cause flux effects, but it is beyond the scope of this study. To reach a complete description of the irradiated microstructure, it is obviously necessary to apply a multitude of complementary techniques, such as atom probe tomography (APT) [10,11], positron annihilation spectroscopy (PAS) [12,13], small-angle neutron scattering (SANS) [14,15] and transmission electron microscopy (TEM) [16,17].

As the irradiation response of RPV steels is typically studied using accelerated irradiations, knowledge on the effect of the neutron flux on the irradiation-induced microstructure

and mechanical properties [10,18–25] is key. All reported results agree on the operation of a pronounced flux effect on the size of irradiation-induced solute atom clusters, while, for the cluster volume fraction, cases of both no flux effect [19] and significant flux effect [23] were reported. Within the paradigm of the mechanical properties being determined by the microstructure, it is still puzzling why, at constant neutron fluence, the irradiated microstructure markedly depends on the neutron flux, while the irradiation-induced mechanical property changes exhibit moderate or even negligible flux dependencies within wide limits of flux [7,18,19,23].

To tackle this issue in more detail, an RPV base and weld material neutron-irradiated at different neutron fluxes up to similar levels of fluence were selected for a collaborative effort. The flux-dependent irradiated microstructures were characterized using APT, PAS, SANS and TEM. In the present contribution, the results are reported, critically assessed and correlated with irradiation hardening in terms of the increase of Vickers hardness.

2. Materials and Methods

The materials investigated in this study are RPV base metals and welds; they are labeled BH (base metal, high flux), BL (base metal, low flux), WH (weld, high flux) and WL (weld, low flux). For cross reference, e.g., [26], these materials are identical with ANP-3, ANP-10 (both 22NiMoCr3-7 type RPV steels), ANP-6 and VFAB-1 (both S3NiMo-type RPV welds), respectively. All materials were provided by Framatome as part of the EU project SOTERIA. The initial microstructure of the base metals is bainitic. The compositions are summarized in Table 1, and the irradiation conditions are shown in Table 2. It is important to note that the irradiation parameters may differ slightly from sample to sample of one material. If not otherwise stated, we use average values of the parameters based on the assumption that the neutron flux, which varies by more than one order of magnitude between “L” and “H”, is the primary variable. Moreover, the low- and high-flux conditions, although produced by the same manufacturers using the same technologies, are from different batches and exhibit certain differences in the composition, e.g., 0.015 versus 0.006% P for the base metals or 1.69 versus 1.2% Ni for the welds. These differences have to be taken into account in the discussion.

Table 1. Bulk composition in mass% (balance Fe).

Material	C	Mn	Si	Cr	Ni	Mo	P	Cu
BH	0.23	0.70	0.20	0.44	0.98	0.79	0.015	0.12
BL	0.18	0.81	0.15	0.40	0.96	0.53	0.006	0.09
WH	0.05	1.41	0.15	0.07	1.69	0.46	0.012	0.08
WL	0.06	1.66	0.21	0.14	1.2	0.80	0.016	0.06

Table 2. Irradiation conditions (neutron energy $E > 1$ MeV).

Material	Fluence (10^{19} cm $^{-2}$)	Flux (10^{12} cm $^{-2}$ s $^{-1}$)	Temperature (°C)	Irradiation Facility *
BH	3.9	1.8	285	VAK
BL	3.4	0.047	300	PWR
WH	5.3	2.3	285	VAK
WL	5.9	0.082	270	BWR

* VAK: Nuclear test facility (BWR type) target channel; Pressurized Water Reactor and Boiling Water Reactor surveillance channel.

All samples, including unirradiated reference samples, were prepared from broken halves of tested fracture mechanics specimens. PAS, SANS and Vickers hardness testing were carried out one after the other using the same samples, measuring $10 \times 10 \times 1$ mm 3 . We note that SANS and gamma-induced positron annihilation spectroscopy (GiPS) are bulk methods, the latter being different from traditional PAS. Therefore, no special surface preparation was required after cutting. For APT, the tips were prepared by two-step

electropolishing from 10-mm-long rod-like samples, five for each material condition. For the first step, 10% perchloric acid with a 90% acetic acid solution was used. For the second step, the solution consisted of 2% perchloric acid and 98% butoxyethanol. For TEM, discs of 3 mm diameter were punched out from the delivered 0.3-mm-thick plates and polished until a thickness of around 0.1 mm was reached. The final electropolishing, up to electron transparency, was performed in a Tenupol 5 machine, using a solution of 5% perchloric acid in methanol at $-60\text{ }^{\circ}\text{C}$.

APT experiments were performed using a LEAP 4000 X HR from Cameca. All tips were analyzed in voltage mode, using a pulse fraction between 15 and 20%. The cooling temperature was set to 50 K, resulting in a tip temperature of 57 K. A 3D reconstruction was done using the IVAS 3.8 software. Reconstruction parameters were determined using the atomic planes spacing. A further data treatment, i.e., cluster identification, composition measurement and dislocation identification, was done using the GPM_3D software. For composition measurements from mass spectra, the noise was removed using the filtering options. Cluster identification was made using the isoposition method (IPM) described in [27]. The elements used for IPM were Cu, Ni and Si. The concentration threshold was set to the value for which the concentration histogram of a randomized data set is negligible ($<0.01\%$). To determine the cluster size, an erosion is applied after the cluster identification. The erosion distance was set at half the maximum of the erosion profile. A second erosion was applied in order to measure the core composition of the clusters. The second erosion distance was set at the edge of the plateau of the solute concentration profile. The segregation along the dislocation lines was identified using phosphorous as the element for IPM.

Lifetime measurements by means of gamma-induced positron annihilation spectroscopy (GiPS) [28,29] were performed at the ELBE pulsed linear electron accelerator at Helmholtz-Zentrum Dresden-Rossendorf [30]. This variant of PAS is particularly well adapted to radioactive neutron-irradiated samples. The electron beam gives rise to the formation of an energetic pulsed γ beam known as bremsstrahlung, from which positrons are generated inside the bulk of the sample via electron-positron pair formation. Each sample was wrapped in Hostaphan foil and fixed on thin threads to minimize the background signals. Characteristic annihilation quanta were registered in coincidence by two pairs of high-purity Germanium semiconductors for accurate energy determination and BaF_2 scintillation detectors for accurate timing, and two pairs of LaBr_2 and BaF_2 detectors. After data compilation, and the coincidence set with the highest counting rate was selected for further analysis. The measured lifetime spectra were analyzed with a three-component fit using the software PALSfit [31].

Magnetic SANS [14] was applied at the instrument V4 at Helmholtz-Zentrum Berlin (HZB). The samples were placed in a magnetic field of 1.5 T perpendicular to the incident neutron beam, with a wavelength of 0.6 nm. Two sample-detector distances of 1.7 and 8 m were chosen to cover a range of scattering vectors Q from 0.1 to 3 nm^{-1} . The data were analyzed using the BerSANS software package [32]. The scattering cross-sections of the unirradiated reference samples were subtracted from the respective cross-sections of the irradiated samples in order to derive the characteristics of irradiation-induced scatterers. Assuming nonmagnetic scatterers, these difference-scattering curves were transformed into size distributions of scatterers using the Monte Carlo method [33].

A TEM [16,17,34] examination was performed in a 200 kV JEOL JEM-2010 device equipped with a LaB_6 filament. Imaging was performed using diffraction contrast, in bright field (BF) and weak beam dark field (WBDF) conditions. The neutron-irradiated materials were examined to look for the presence of features that could be dislocation loops produced by neutron irradiation. It is important to note that, under the present irradiation conditions, loops were rarely observed and appeared as black dots mostly placed close to pre-existing line dislocations. The procedure of analysis was adapted to this situation. Particular attention was paid to distinguish dislocation loops from other features with similar contrast, such as precipitates or dislocation line junctions. With that purpose, the

TEM samples were tilted to provide a good diffraction contrast for dislocations, using two beam conditions by exciting the reflections $g = 110$ and $g = 200$, close to $[111]$, $[110]$ and $[100]$, if possible. WBDF images taken at different tilting conditions were compared with BF images. The information given in this study consists of a qualitative description of the irradiation-induced microstructure and the quantification of the features identified as dislocation loops in terms of average diameter and number density. The loops were counted and divided by both the analyzed area and the estimated foil thickness in order to obtain average number densities.

Vickers hardness HV10 (load 98.1 N) was measured using the SANS samples after completion of the SANS experiments. The given HV10 values are the mean value and standard deviation from 10 hardness tests per sample, from which the irradiation-induced hardness increase was derived. The distance between individual hardness indentations was greater than 1 mm (more than three times the indentation size).

3. Results

3.1. Positron Lifetime

The measured lifetime spectra in terms of counts per lifetime increment are shown in Figure 1a for the RPV base material irradiated at low flux (BL) and high flux (BH), along with the unirradiated reference (BU).

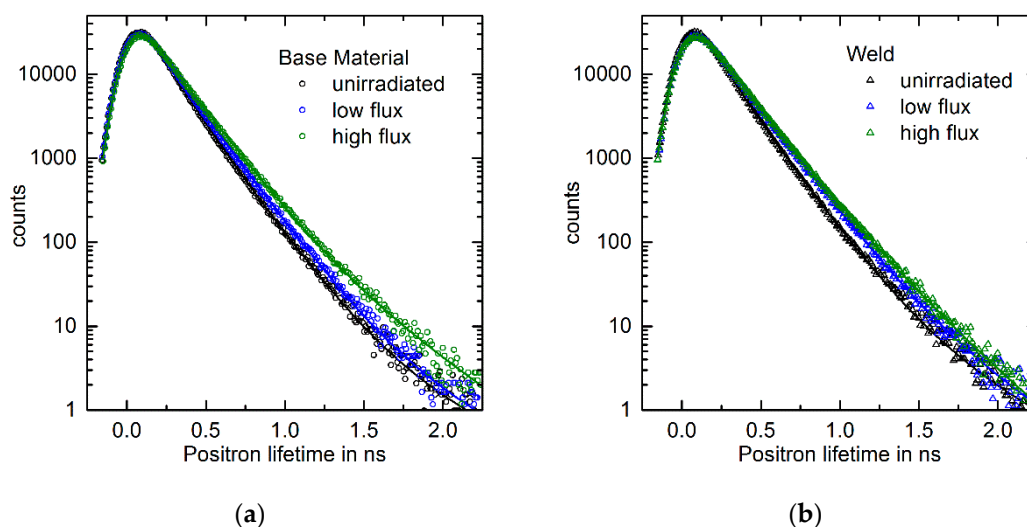


Figure 1. Measured lifetime spectra and fitted three-component models for (a) a low-flux (BL) and high-flux (BH) condition of the RPV base material, along with the unirradiated reference (BU); (b) a low-flux (WL) and high-flux (WH) condition of the RPV base material along with the unirradiated reference (WU).

The spectra were decomposed into three lifetime components, each component being characterized by a lifetime and an associated intensity. Two of the lifetimes (but not the intensities) were fixed according to prior knowledge, namely the lifetimes 108 ps for annihilation events in bulk bcc iron [13] and 175 ps for annihilation events in single vacancies [35]. The remaining four parameters (one lifetime and three intensities) were determined by fitting the three-component model to the measured lifetime spectra. The same procedure was applied to the RPV weld (Figure 1b).

The derived best-fit parameters are summarized in Table 3.

We have observed that the mean lifetime increases in the order U-L-H for both the RPV base material and the weld. The intensity of the third lifetime (the highest one among the three components) also increases in the same order. The third lifetime is likely due to vacancy clusters [35]. The results are consistent with the following interpretation: Irradiation-induced vacancy clusters consisting of a number of vacancies between 9 (lifetime

approximately 280 ps) and 25 (lifetime approximately 390 ps), on average [35], are formed. A possible exception is condition BL, for which the intensity is only slightly larger than for BU (0.44% versus 0.32%). It is important to note that vacancy clusters containing 25 vacancies are still sub-nanometric in size. The higher intensities observed for the high-flux conditions indicate a higher number density of such clusters as compared to the lower flux. The intensity of the second (fixed) lifetime component, here interpreted as due to single vacancies, indicates a higher concentration of irradiation-induced vacancies for BH as compared to BL. For the weld material, the fitted intensity for WH is smaller than for WL, but at levels close to 100% for both conditions. In the summary of the positron lifetime measurements, we conclude that a higher concentration of sub-nm-sized vacancy clusters is formed for the high-flux conditions of both materials. Such vacancy clusters may be associated with solute-atom clusters, as demonstrated by Kuriplach et al. for the case of Cu-rich clusters [35].

Table 3. Best-fit parameters derived for the three-component model with two fixed lifetimes.

Material/ Condition	Component 1 (108 ps, Fixed) Intensity (%)	Component 2 (175 ps, Fixed) Intensity (%)	Component 3 (Fitted) Lifetime (ps)	Component 3 Intensity (%)	Mean Lifetime (ps)
BU	45.02	54.66	492	0.32	146
BL	22.49	77.07	462	0.44	161
BH	3.82	92.35	347	3.83	179
WU	38.76	60.64	445	0.60	151
WL	0	98.56	374	1.44	178
WH	0	92.08	282	7.92	183

3.2. TEM

For nm-sized interstitial clusters, planar arrangements known as dislocation loops are energetically favorable over 3D arrangements. Using diffraction contrast, such loops can be characterized by means of TEM. Figure 2a,b shows WBDF TEM micrographs for the high-flux irradiation (BH) and low-flux irradiation (BL), respectively, of the RPV base material. The arrows indicate loops appearing as white dots. It is worth pointing out that such white dots were not observed in the unirradiated samples. The coarse microstructure (the grain and dislocation structure, as well as the carbide/carbonitride initial phases) is expected not to have been affected by neutron irradiation at the irradiation conditions considered.

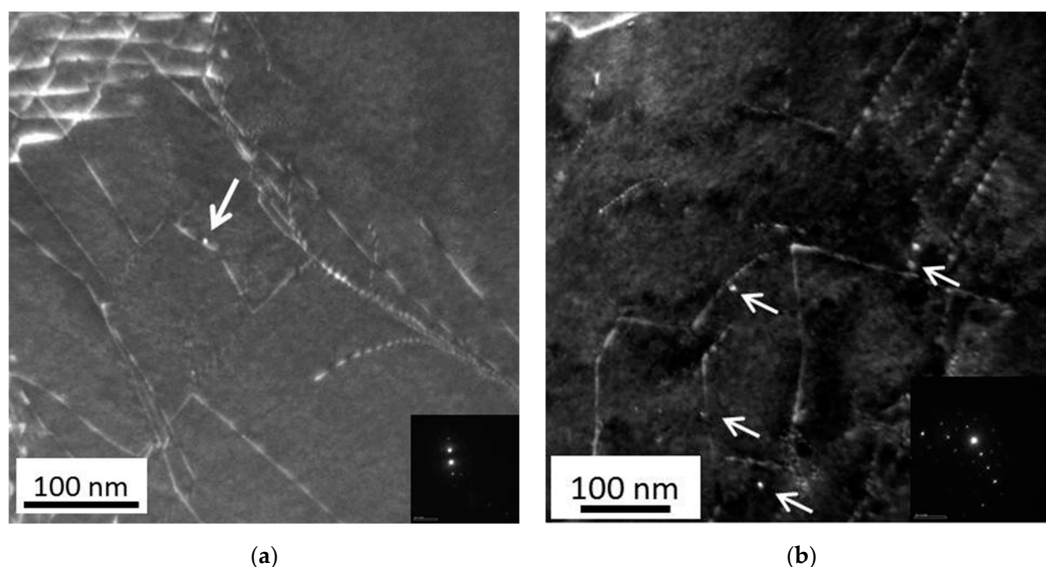


Figure 2. WBDF TEM image for the RPV base material, (a) high-flux condition (BH), (b) low-flux condition (BL). $g = 110$. Features identified as dislocation loops are marked with an arrow.

The same kind of information for welds is shown in Figure 3. For each studied material, several micrographs of larger magnification, together covering larger areas, were analyzed for loop identification, sizing and counting. Estimates of the mean diameter and number density of loops are summarized in Table 4. It is important to note that the identified dislocation loops were preferentially located close to pre-existing line dislocations, meaning that the spatial distribution of loops is inhomogeneous. The averaged number densities were estimated as the number of counted loops divided by the total analyzed area and the foil thickness (100 nm).

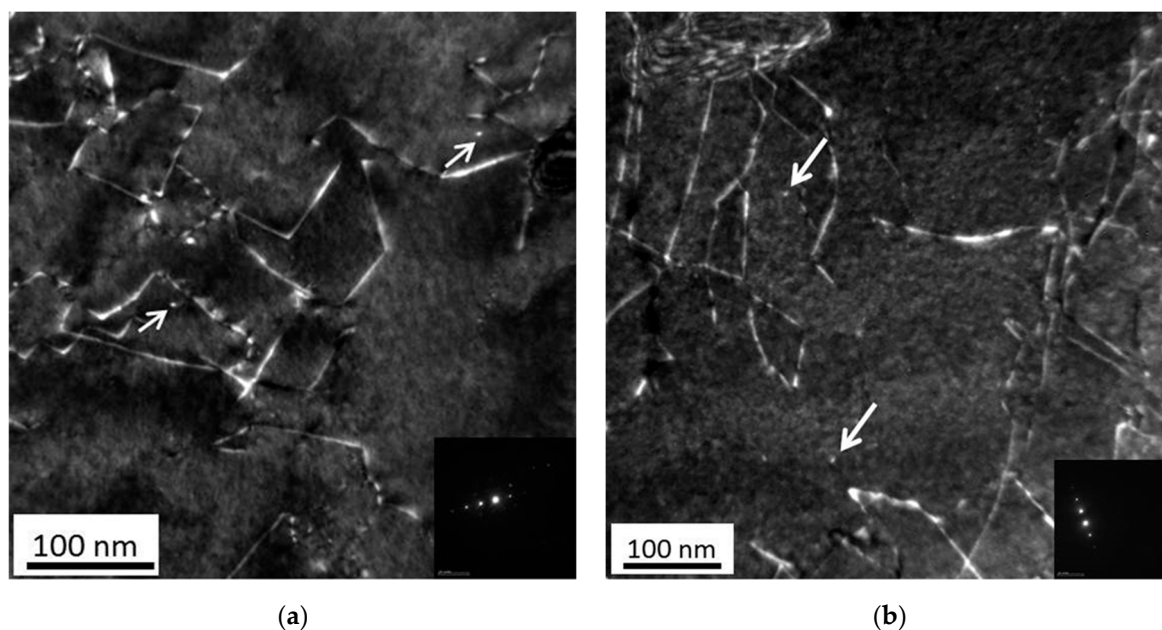


Figure 3. WBDF TEM image for the RPV weld, (a) high-flux condition (WH); (b) low-flux condition (WL). $g = 110$. Features identified as dislocation loops are marked with an arrow.

Table 4. Estimates of the mean diameter and number density of dislocation loops.

Material	Number of Sized Loops	Mean Diameter (nm)	Loop Density (10^{20} m^{-3})
BH	3	3.8 ± 0.3	0.08 ± 0.04
BL	34	4.0 ± 0.2	2.0 ± 0.3
WH	33	3.8 ± 0.1	1.7 ± 0.5
WL	15	3.4 ± 0.9	1.2 ± 0.5

We have found that the mean diameter of loops agrees within the error margin for all samples studied and is close to 4 nm. The number density of loops is relatively small (as compared to solute clusters, see next section) for all samples. It is, therefore, risky to draw conclusions about the trends. For the RPV base material, the low flux gives rise to a significantly higher loop density than the high flux. For the weld, the loop densities (WH versus WL) agree within the error margin and are closer to the low-flux condition of the base material (BL).

3.3. APT

APT is capable of providing rich information on the local microstructure of unirradiated and irradiated materials including the depletion or enrichment of certain volumes with solute atoms and their spatial correlations with features of the initial microstructure. An example encountered with the samples of this study is the segregation of phosphorous on pre-existing line dislocations. The present study is focused on the composition, size

and number density of irradiation-induced solute clusters as a function on neutron flux. One of the reconstructed solute atom maps obtained for the high-flux irradiation of the RPV base material (BH) is shown in Figure 4 as an example. A high number density of Cu-Ni-Si-Mn-enriched clusters randomly distributed in the matrix is visible. It is interesting to note that such clusters with slightly different size and composition were also observed in close vicinity to the dislocation lines.

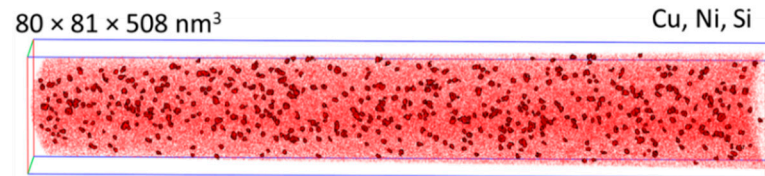


Figure 4. APT solute atom map for the RPV base material irradiated at high flux (BH). Cu, Ni and Si atoms are represented in red. Clusters are highlighted using a threshold of 3.6 at%.

One of the corresponding atom maps derived for the low-flux condition BL of the same type of base material is shown in Figure 5. Again, the map reveals a high number density of Cu-Ni-Si-Mn-enriched clusters dispersed in the matrix. Finally, Figure 6 shows the corresponding atom maps for the high- (WH) and low-flux (WL) conditions of the weld.

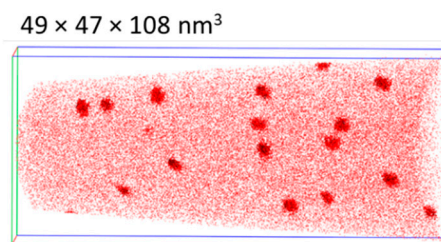


Figure 5. APT solute atom map for the RPV base material irradiated at low flux (BL). Cu, Ni and Si atoms are represented in red. Clusters are highlighted using a slightly higher threshold of 5.2 at%.

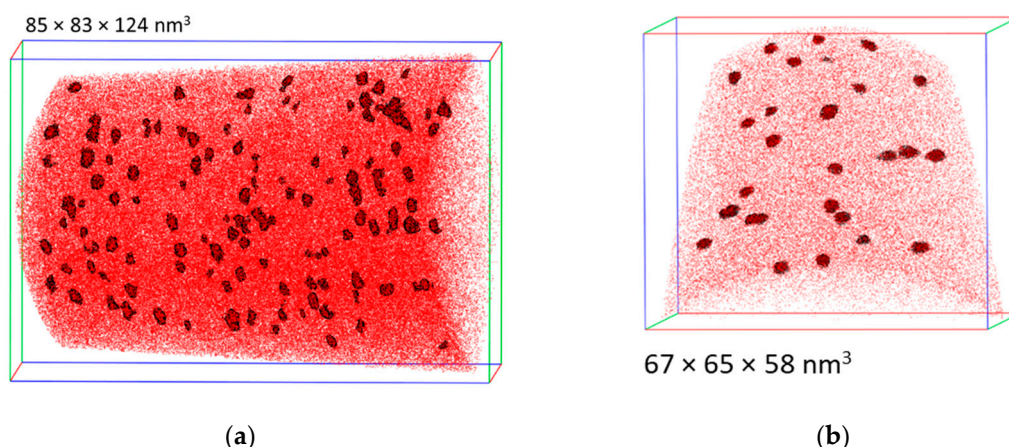


Figure 6. APT solute atom map for the RPV weld, (a) high-flux condition (WH), (b) low-flux condition (WL). Cu, Ni and Si atoms are represented in red. Clusters are highlighted using thresholds of 5.6 and 5 at% for WH and WL, respectively.

In total, either two or three tips were analyzed for each material, representing the total numbers of atoms between 6×10^6 and 116×10^6 . The mean compositions of the solute atom clusters dispersed in the matrix are summarized in Table 5. The mean size and number density of those clusters are reported in Table 6. The element with the highest absolute concentration in the solute atom clusters, apart from Fe, is Ni for all materials. The

enrichment factor is generally higher for Cu. The clusters for both high-flux conditions (BH and WH) contain more Fe and exhibit a higher dilution than the respective low-flux conditions. The number density of clusters for condition BH is higher and the size smaller than for BL. For the welds, cluster size and number density agree within the error margin and are closer to the high-flux condition of the RPV base material.

Table 5. Solute atom cluster composition in at%. Only elements with significant absolute amounts (>1%) and enrichment factors (>2) are listed; the enrichment factors are given in parentheses.

Material	Mn	Si	Ni	P	Cu
BH	2.6 (6.2)	3.5 (8.7)	6.3 (8.0)	0.18 (32)	5.3 (118)
BL	10.8 (15)	9.0 (36)	21 (23)	0.10 (100)	6 (133)
WH	3.0 (4.7)	5.4 (10)	7.2 (9.1)	0.14 (77)	1.6 (35)
WL	9.1 (9.8)	5.8 (12)	11.5 (23)	0.24 (40)	8.8 (243)

Table 6. Estimates of the mean diameter and number density of solute atom clusters located in the matrix. Errors are sample-to-sample variations.

Material	Mean Diameter (nm)	Number Density (10^{23} m^{-3})
BH	2.7	3.7 ± 0.5
BL	3.2	1.1 ± 0.3
WH	2.6	3.1 ± 0.4
WL	2.8	3.0 ± 1.4

3.4. Magnetic SANS

Magnetic SANS allows macroscopically representative (probed volume approximately 50 mm^3) and statistically reliable (typical number of scattering events of 10^6) estimates of size, volume fraction and number density to be derived, the latter two on the assumption of nonmagnetic scatterers. If the scatterers bear a nonvanishing average magnetic moment, the volume fraction and number density are systematically underestimated. The measured magnetic scattering cross sections and reconstructed size distributions are shown in Figures 7 and 8 for the RPV base material and weld, respectively.

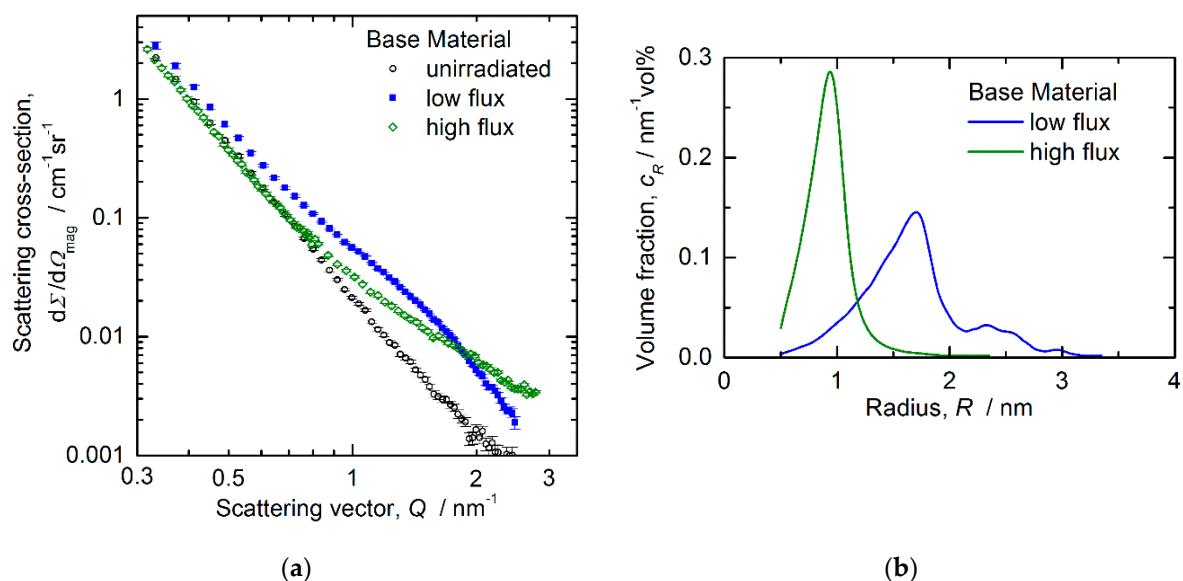


Figure 7. Results from magnetic SANS for the RPV base material, (a) magnetic scattering cross sections, (b) reconstructed size distributions of irradiation-induced scatterers.

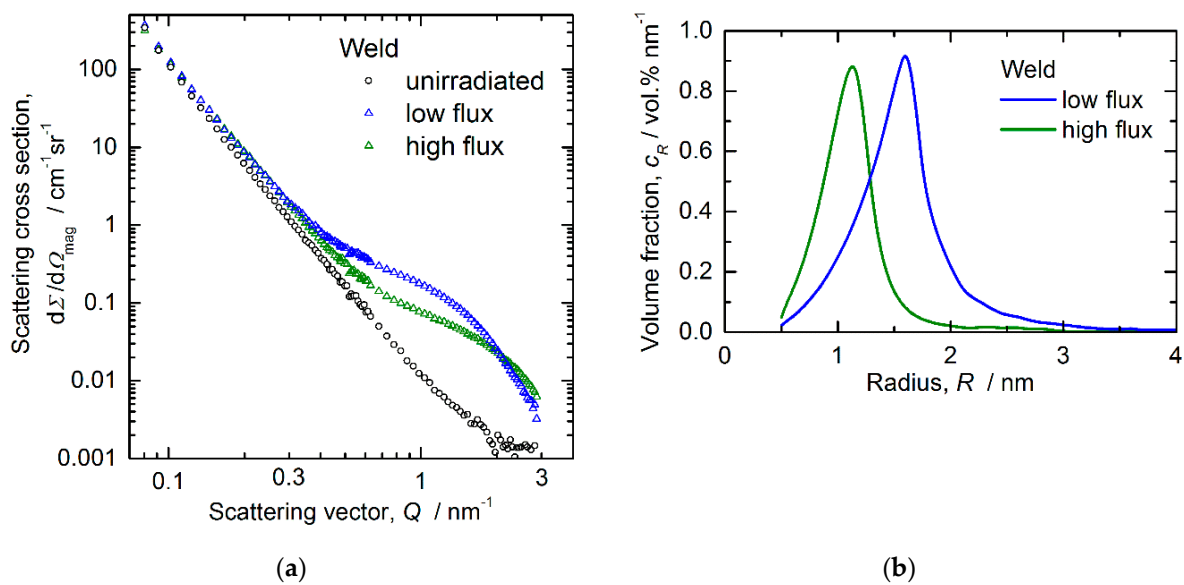


Figure 8. Results from magnetic SANS for the RPV weld, (a) magnetic scattering cross sections, (b) reconstructed size distributions of irradiation-induced scatterers.

The size distributions plotted in Figures 7b and 8b were derived from the magnetic difference scattering curves with the unirradiated samples taken as reference. Table 7 summarizes the mean size of scatterers derived from magnetic SANS along with the volume fraction and number density of scatterers, both estimated on the assumption of nonmagnetic scatterers. The measured average ratio of magnetic (M) and nuclear (N) scattering is also given in terms of the so-called A-ratio, $A = 1 + M/N$.

Table 7. Estimates of the mean diameter, volume fraction, number density and A-ratio of irradiation-induced scatterers derived from magnetic SANS.

Material	Mean Diameter (nm)	Volume Fraction (%)	Number Density (10^{23} m^{-3})	A-Ratio (-)
BH	1.58 ± 0.04	0.124 ± 0.005	5.0 ± 0.4	2.6 ± 0.1
BL	2.46 ± 0.06	0.120 ± 0.014	1.1 ± 0.1	2.5 ± 0.1
WH	1.80 ± 0.06	0.534 ± 0.016	13.0 ± 1.5	2.2 ± 0.1
WL	2.32 ± 0.04	0.710 ± 0.002	7.5 ± 0.3	2.2 ± 0.1

It is reasonable to assume that the irradiation-induced scatterers represent the same family of nanofeatures identified by means of APT as Cu-Ni-Si-Mn-enriched clusters. The number densities estimated for the high-flux conditions of both materials are higher and the sizes are smaller as compared to the respective low-flux conditions. These trends are partly canceled out in the volume fractions, for which the differences are less pronounced. The A-ratio as a one-parameter indicator of composition does not significantly depend on flux. It is important to note that a hypothetical addition to the clusters (or removal from them) of Fe atoms bearing the same magnetic moment as Fe atoms in the matrix does not give rise to any changes of the A-ratio.

3.5. Mechanical Properties

The results of the Vickers hardness tests, namely the mean value and standard deviation from 10 tests each, are compiled in Table 8. We emphasize that Vickers hardness testing was performed on the SANS samples, which largely excludes inconsistency due to possible material inhomogeneity. Moreover, both hardness tests and SANS probe comparable macroscopic volumes.

Table 8. Measured Vickers hardness HV10 (load 98.1 N) and its irradiation-induced change.

Material	HV10	Δ HV10
BU	$184 \pm 3/196 \pm 4^*$	-
BH	238 ± 5	54 ± 6
BL	220 ± 5	24 ± 7
WU	$209 \pm 3/213 \pm 4^*$	-
WH	307 ± 8	98 ± 9
WL	302 ± 6	89 ± 8

* First and second data correspond to the heats irradiated at high and low flux, respectively.

All measurements indicate irradiation hardening. For the RPV base material, hardening appears to be larger for the high-flux irradiation. The smaller fluence (by 13%, see Table 2) received by the low-flux sample of the base material cannot explain the difference. For the RPV weld, and the hardening levels for low and high flux agree within the error margin.

4. Discussion

4.1. Complementarity of Methods and Overlap of Information

The applied methods of microstructure characterization exhibit a high degree of complementarity with each other with respect to the identified types of nanofeatures. Indeed:

- PAS is preferable to gain information about vacancy-type defects. We have found that neutron irradiation gives rise to increased concentrations of single vacancies and sub-nm vacancy clusters and that the higher flux results in higher intensities of the vacancy-cluster component.
- TEM is unique in providing insight on the formation of dislocation loops and their spatial correlations with pre-existing line dislocations. For the RPV base material (but not for the weld), the higher flux results in a lower number density of loops.
- APT resolves the composition of irradiation-induced solute atom clusters and segregations. Moreover, spatial correlations of clusters/segregations with pre-existing dislocations and grain boundaries are accessible. In short, the irradiation-induced solute atom clusters are more diluted for the high-flux condition.
- Magnetic SANS is capable of providing macroscopically representative and statistically reliable estimates of cluster size and volume fraction. The most prominent finding is the detection of significantly smaller cluster sizes for the high-flux irradiations.

The same methods also allow overlapping information to be extracted. It is important to emphasize that such cases of overlap are not just redundancies. In fact, they can be actively used to cross-check estimates derived from different methods and gain additional information. A number of (possible or real) overlaps is briefly addressed below:

- Vacancy clusters may be associated to solute atom clusters [36]. Therefore, it is possible that the sub-nm vacancy clusters detected by PAS, although in themselves smaller than the lower detection limit of SANS, also contribute to the cluster characteristics as extracted from SANS. That means that those vacancy clusters might have slightly raised the volume fraction and reduced the A-ratio.
- Initially mobile dislocation loops may encounter solute atoms, get immobilized and turn, via solute segregation, into solute atom clusters. Indeed, this process was identified as the dominant formation mechanism of irradiation-induced solute atom clusters [5]. This means that part of the loops identified by TEM might also contribute to the estimates derived by APT or SANS for solute atom clusters.
- APT and SANS exhibit overlapping information with respect to the size and number density of solute atom clusters [11]. Moreover, the cluster composition derived from APT can be used to estimate the expected theoretical A-ratio of SANS. The latter option is not used here for the sake of conciseness.

The mean cluster diameters and number densities derived from APT and SANS can be compared based on the data provided in Tables 6 and 7. We find that SANS tends to

indicate smaller clusters (30% difference, on average) and higher number densities (factor 2, on average, agreement for BL) than those derived from APT. The smaller size is reasonable, because APT reveals a substantial contribution of Fe atoms to the clusters, while scattering is due to the amount of difference between cluster and matrix. As the most robust estimate from SANS is volume fraction, the higher number density at a given volume fraction may be a consequence of the smaller size. Taking into account this kind of bias in the estimates derived from different methods, the whole set of results tends to be consistent.

It is important to remind here that the SANS estimates of volume fraction and number density are based on the assumption of nonmagnetic clusters in the ferromagnetic matrix. A possible violation of this assumption, however, would give rise to a decrease of the magnetic contrast and to related increases of the estimates of volume fraction and number density, which means the opposite of what would be necessary to harmonize the number densities from both methods. We conclude that the possible magnetism of the clusters, if any, cannot be the dominant source of the deviation between the number densities from SANS and APT.

4.2. Flux effect on Microstructure

Taking into account the full set of applied methods, we have found significant flux effects for both the RPV base material and the weld. For the base material, the higher flux (flux lead factor of 38 at comparable fluence) gives rise to

- a higher number density of sub-nm vacancy clusters,
- a lower number density of nm-sized loops, and
- a higher number density of smaller and more diluted solute atom clusters.

For the weld materials, the higher flux (flux lead factor of 28 at comparable fluence) gives rise to

- a higher number density of sub-nm vacancy clusters,
- a comparable size and number density of nm-sized loops, and
- a higher number density of smaller and more diluted solute atom clusters.

For more details, see Section 3. The pronounced dependence of the cluster size on flux was reported and rationalized before in terms of the flux-dependent point-defect balance [18,19] and deterministic cluster growth according to the Johnson-Mehl-Avrami-Kolmogorov kinetics model [18,37–39]. The size measurements by SANS as a function of flux are summarized in Figure 9 with an additional data point reported before for medium flux [40] (code P151GW). The dashed line corresponds to the model based on deterministic growth [23]. Figure 9 demonstrates the consistence between old and new measurements, between behaviors for base and weld, and between model and experiment, thus confirming the previous conclusions.

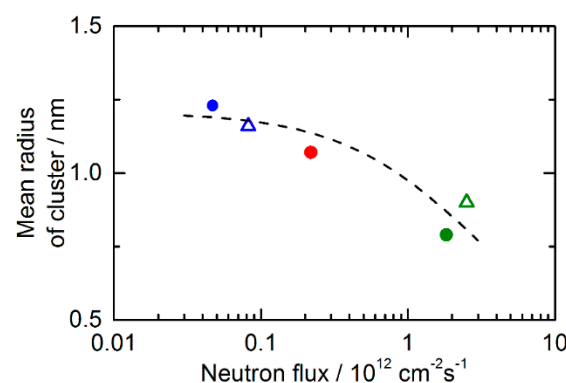


Figure 9. Cluster radius by SANS as a function of flux. The base material is indicated by the full circles, and the weld by the open triangles. The data point for the same RPV base material is indicated by the red dot from [40]. The dashed line corresponds to the model based on deterministic growth [23].

The dependence of the cluster volume fraction on flux does not seem to exhibit a unique behavior. For the RPV base material, the volume fractions derived from SANS for the two fluxes agree within the error margin. By contrast, the higher flux results in a smaller volume fraction for the weld. The former finding is compatible with the independence of flux reported in [19] in a single case, and the latter agrees with the general trend found in [23]. Modeling the kinetics of cluster evolution [23] indicated that the independence of flux is consistent with Ostwald ripening, whereas a decrease of volume fraction at increasing flux is consistent with deterministic growth. Based on the general trend [23] and the reported applicability of deterministic growth [23,38,39], we conclude that the flux-independent volume fraction observed for the base material is an artifact due to both the experimental error of the measured volume fraction and minor differences in the total fluence. Indeed, the error ranges alone would allow for a 20% smaller volume fraction for the higher flux. Moreover, the total neutron fluence reached for the high-flux irradiation (Table 2) was somewhat larger, meaning that the respective volume fraction has to be corrected towards smaller values. In summary, the present observations for the volume fraction are essentially consistent with the mechanism of deterministic growth and volume fractions decreasing at increasing flux.

With respect to the cluster composition, the dominant effect of flux is a higher degree of dilution for the higher flux (that is, a larger Fe fraction as indicated by APT).

The observed contribution of vacancy-type defects, be it in the form of single vacancies, vacancy solute complexes or sub-nm vacancy clusters, increases at an increasing neutron flux, as supported by both the mean positron lifetime and the intensity of the third lifetime component. This finding is qualitatively consistent with the point-defect balance under neutron irradiation [19,41,42]. Indeed, a naïve (that means, assuming a constant sink strength) application of the rate equations indicates that the vacancy concentration under irradiation approaches a steady state and that the steady-state concentration exhibits a linear and square-root dependence on flux in the low-flux and high-flux regime, respectively. The transition flux was estimated to be in the order of $10^{12} \text{ cm}^{-2} \text{ s}^{-1}$ [19], that is, the low and high flux applied in this study are below and above the transition flux, respectively. In reality, the effect of flux on the vacancy concentration is still present, but, because of the evolving sink strength, it is weaker than naïvely predicted [18,41], which means that it is closer to our observation.

The TEM results in this study indicate a smaller number density of dislocation loops for the RPV base material irradiated at the higher flux. This seems to be counterintuitive with respect to the point-defect balance discussed above for vacancies. However, we have to take into account the following limitations:

- Measurements of the concentration of single self-interstitial atoms are not available.
- Loops of diameter smaller than approximately 1.5 nm are TEM-invisible.
- Loops may transform into 3D solute atom clusters [5] (see above) and lose the loop-typical diffraction contrast.

A comparison of the TEM observations with simplified rate theory models is beyond the scope of this study. It remains to be clarified why loops appear close to dislocation lines (finding from TEM), while solute atom clusters, which were claimed to develop from loops [5], appear throughout the matrix (finding from APT).

4.3. Flux Effect on Hardening

The results of this study show that the dominant hardening nanofeatures are the Cu-Ni-Si-Mn-enriched clusters identified by APT. Indeed, the family of dislocation loops resolved by TEM is characterized by a number density that is smaller by three or more orders of magnitude, and the family of vacancy clusters identified by GiPS is of sub-nm size and may be associated with solute atom clusters. It is, therefore, natural to estimate

the hardness increase expected solely taking into account the family of solute atom clusters. We have applied the dispersed barrier hardening (DBH) model in its original form [43],

$$\Delta HV10 = \alpha \beta M G b \sqrt{N d}, \quad (1)$$

where the number density N and mean diameter d were taken from the SANS experiments (Table 7), as they represent the same samples and approximately the same macroscopic volumes as covered by Vickers hardness testing. The parameters α , β , M , G and b represent the dimensionless obstacle strength, the conversion factor between yield stress and Vickers hardness number, the Taylor factor ($M = 3.06$), the shear modulus ($G = 84$ GPa) and the magnitude of the Burgers vector ($b = 0.248$ nm), respectively. A reasonable estimate of the dimensionless obstacle strength of Cu-Ni-Si-Mn-enriched clusters is $\alpha = 0.1$ [44]. The conversion factor from yield stress (in MPa) to the Vickers hardness number can be approximated as $\beta = 3/9.81 = 0.306$ [45]. Figure 10 demonstrates a good correlation between the measured increase of hardness and the estimates based on Equation (1).

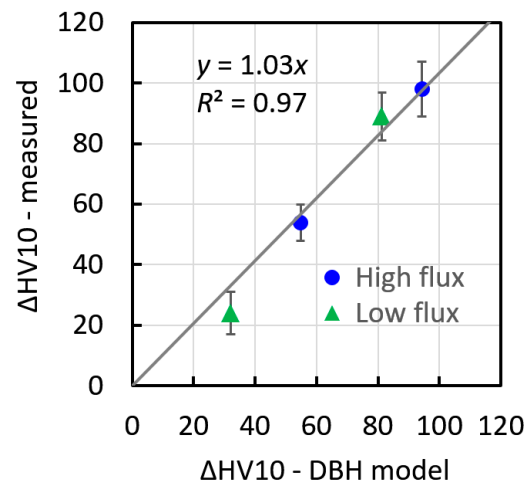


Figure 10. Comparison of the Vickers hardness increase estimated within the DBH model, Equation (1), with the measured Vickers hardness increase for the four RPV materials covered in this study. The triangles (dots) refer to the base (weld) materials.

We have found that there is a systematic, but—in view of the pronounced flux effect on the size and number density of solute atom clusters—relatively minor effect of flux on irradiation hardening. This is a consequence of the flux effects on size and number density being in opposite directions and partly canceling out in Equation (1).

It is particularly interesting to see that the low-flux data (green triangles) and the high-flux data (blue circles) are equally well represented by Equation (1) using a common set of parameters. We conclude that the observed flux effect on the Vickers hardness results from the flux effects on the cluster size and number density as derived from magnetic SANS assuming nonmagnetic scatterers. However, we cannot exclude the possibility that the assumption of nonmagnetic scatterers gives rise to an underestimation of the cluster number density for the higher flux compensated by an overestimation of the obstacle strength because of the higher dilution. The fact that the intersection of the regression line in Figure 10 is not significantly greater than zero confirms that nanofeatures not detected by SANS (such as loops or sub-nm vacancy clusters) do not contribute significantly to hardening.

5. Conclusions

We have applied APT, PAS/GiPS, SANS and TEM in order to uncover flux effects on the irradiation-induced nanofeatures in neutron-irradiated RPV steels and welds. Several types of irradiation-induced nanofeatures have been identified, such as vacancy clusters,

dislocation loops, solute atom clusters and segregations to dislocations. Solute atom clusters have been found to be smaller, more diluted and with a higher number density for the high-flux conditions of both the base and the weld material. The DBH model provides a link between the microstructure and irradiation hardening in terms of Vickers hardness. It has been demonstrated that the measured Vickers hardness increase, including the flux effect, is well reproduced based on SANS estimates of size and number density of solute atom clusters along with reasonable values of the model parameters. The relatively minor flux effect on hardening is due to opposite flux effects on size and number density. While the accelerated irradiation gives rise to a higher hardness increase in the present case, we cannot generalize this finding. Such effort would require corrections for different compositions and, more importantly, the consideration of non-hardening embrittlement [6–9].

Author Contributions: Conceptualization, A.U., M.H.-M., B.R., H.H. and F.B.; methodology, A.U., M.H.-M., B.R., E.H., A.W. and F.B.; formal analysis, A.U., M.H.-M., E.O., A.E., B.R., E.H., A.W. and F.B.; investigation, A.U., M.H.-M., E.O., A.E., B.R., E.H. and A.W.; resources, A.U., M.H.-M., B.R. and H.H.; data curation, A.U.; writing—original draft preparation, A.U. and F.B.; writing—review and editing, A.U., M.H.-M., E.O., A.E., B.R., E.H., A.W., H.H. and F.B.; visualization, A.U., M.H.-M., E.O., A.E., B.R. and F.B.; supervision, M.H.-M., B.R., A.W. and F.B.; funding acquisition, M.H.-M., B.R., H.H. and F.B. All authors have read and agreed to the published version of the manuscript.

Funding: This work received funding from the European Union’s Horizon 2020 research and innovation program under grant agreement No 661913 “SOTERIA”.

Institutional Review Board Statement: Not applicable.

Informed Consent Statement: Not applicable.

Data Availability Statement: The data supporting the reported results were obtained within the European Union’s Horizon 2020 project “SOTERIA”, for further information see www.soteria-project.eu (accessed on 19 January 2022). The data are included in several project deliverables, and they will be provided by the authors upon reasonable request.

Acknowledgments: We would like to acknowledge SANS beamtime and the technical support by Uwe Keiderling at the instrument V4 at Helmholtz-Zentrum Berlin (HZB). Special thanks to Maik Butterling for insightful discussions on the PAS results and to Michaela Rossner for Vickers hardness testing.

Conflicts of Interest: The authors declare no conflict of interest.

References

1. Odette, G.R. On the Dominant Mechanism of Irradiation Embrittlement of Reactor Pressure Vessel Steels. *Scr. Metall.* **1983**, *17*, 1183–1188. [[CrossRef](#)]
2. Auger, P.; Pareige, P.; Akamatsu, M.; Blavette, D. APFIM Investigation of Clustering in Neutron-Irradiated FeCu Alloys and Pressure Vessel Steels. *J. Nucl. Mater.* **1995**, *225*, 225–230. [[CrossRef](#)]
3. Odette, G.R.; Lucas, G.E. Recent Progress in Understanding Reactor Pressure Vessel Steel Embrittlement. *Radiat. Eff. Defects Solids* **1998**, *144*, 189–231. [[CrossRef](#)]
4. Meslin, E.; Lambrecht, M.; Hernandez-Mayoral, M.; Bergner, F.; Malerba, L.; Pareige, P.; Radiguet, B.; Barbu, A.; Gomez-Briceno, D.; Ulbricht, A.; et al. Characterization of Neutron-Irradiated Ferritic Model Alloys and a RPV Steel from Combined APT, SANS, TEM and PAS Analyses. *J. Nucl. Mater.* **2010**, *406*, 73–83. [[CrossRef](#)]
5. Castin, N.; Bonny, G.; Bakaev, A.; Bergner, F.; Domain, C.; Hyde, J.M.; Messina, L.; Radiguet, B.; Malerba, L. The Dominant Mechanisms for the Formation of Solute-Rich Clusters in Low-Cu Steels under Irradiation. *Mater. Today Energy* **2020**, *17*, 100472. [[CrossRef](#)]
6. Gurovich, B.; Kuleshova, E.; Shtrombakh, Y.; Fedotova, S.; Maltsev, D.; Frolov, A.; Zabusov, O.; Erak, D.; Zhurko, D. Evolution of Structure and Properties of VVER-1000 RPV Steels under Accelerated Irradiation up to beyond Design Fluences. *J. Nucl. Mater.* **2015**, *456*, 23–32. [[CrossRef](#)]
7. Boåsen, M.; Efsing, P.; Ehrnstén, U. On Flux Effects in a Low Alloy Steel from a Swedish Reactor Pressure Vessel. *J. Nucl. Mater.* **2017**, *484*, 110–119. [[CrossRef](#)]
8. Kuleshova, E.A.; Gurovich, B.A.; Lavrukina, Z.V.; Maltsev, D.A.; Fedotova, S.V.; Frolov, A.S.; Zhuchkov, G.M. Study of the Flux Effect Nature for VVER-1000 RPV Welds with High Nickel Content. *J. Nucl. Mater.* **2017**, *483*, 1–12. [[CrossRef](#)]
9. Wang, K.; Guo, Y.; Song, S. Quantitative Dependence of Ductile-to-Brittle Transition on Phosphorus Grain Boundary Segregation for a Novel Ni–Cr–Mo RPV Steel. *J. Mater. Res. Technol.* **2021**, *15*, 6404–6414. [[CrossRef](#)]

10. Soneda, N.; Dohi, K.; Nishida, K.; Nomoto, A.; Tomimatsu, M.; Matsuzawa, H.; Busby, J.T.; Hanson, B.; Dean, S.W. Microstructural Characterization of RPV Materials Irradiated to High Fluences at High Flux. *J. ASTM Int.* **2009**, *6*, 102128. [[CrossRef](#)]
11. Meslin, E.; Radiguet, B.; Pareige, P.; Barbu, A. Kinetic of Solute Clustering in Neutron Irradiated Ferritic Model Alloys and a French Pressure Vessel Steel Investigated by Atom Probe Tomography. *J. Nucl. Mater.* **2010**, *399*, 137–145. [[CrossRef](#)]
12. Lambrecht, M.; Almazouzi, A. Positron Annihilation Study of Neutron Irradiated Model Alloys and of a Reactor Pressure Vessel Steel. *J. Nucl. Mater.* **2009**, *385*, 334–338. [[CrossRef](#)]
13. Cizek, J.; Procházka, I.; Kocik, J.; Keilová, E. Positron Lifetime Study of Reactor Pressure Vessel Steels. *Phys. Status Solidi A* **2000**, *178*, 651–662. [[CrossRef](#)]
14. Mühlbauer, S.; Honecker, D.; Périgo, É.A.; Bergner, F.; Disch, S.; Heinemann, A.; Erokhin, S.; Berkov, D.; Leighton, C.; Eskildsen, M.R.; et al. Magnetic Small-Angle Neutron Scattering. *Rev. Mod. Phys.* **2019**, *91*, 015004. [[CrossRef](#)]
15. Beaven, P.A.; Frisius, F.; Kampmann, R.; Wagner, R. Analysis of Defect Microstructures in Irradiated Ferritic Alloys. In *Atomic Transport and Defects in Metals by Neutron Scattering*; Janot, C., Petry, W., Richter, D., Springer, T., Eds.; Springer: Berlin/Heidelberg, Germany, 1986; Volume 10, pp. 228–233. ISBN 978-3-642-71009-4.
16. Hernández-Mayoral, M.; Gómez-Briceño, D. Transmission Electron Microscopy Study on Neutron Irradiated Pure Iron and RPV Model Alloys. *J. Nucl. Mater.* **2010**, *399*, 146–153. [[CrossRef](#)]
17. Kirk, M.; Yi, X.; Jenkins, M. Characterization of Irradiation Defect Structures and Densities by Transmission Electron Microscopy. *J. Mater. Res.* **2015**, *30*, 1195–1201. [[CrossRef](#)]
18. Odette, G.R.; Yamamoto, T.; Klingensmith, D. On the Effect of Dose Rate on Irradiation Hardening of RPV Steels. *Philos. Mag.* **2005**, *85*, 779–797. [[CrossRef](#)]
19. Bergner, F.; Ulbricht, A.; Hein, H.; Kammel, M. Flux Dependence of Cluster Formation in Neutron-Irradiated Weld Material. *J. Phys.-Condens. MATTER* **2008**, *20*, 104262. [[CrossRef](#)]
20. Dohi, K.; Nishida, K.; Nomoto, A.; Soneda, N.; Matsuzawa, H.; Tomimatsu, M. Effect of Neutron Flux at High Fluence on Microstructural and Hardness Changes of RPV Steels. In Proceedings of the ASME 2010 Pressure Vessels and Piping Conference, ASMEDC, Bellevue, WA, USA, 18–22 January 2010; Volume 9, pp. 95–102.
21. Chaouadi, R.; Gérard, R. Confirmatory Investigations on the Flux Effect and Associated Unstable Matrix Damage in RPV Materials Exposed to High Neutron Fluence. *J. Nucl. Mater.* **2013**, *437*, 267–274. [[CrossRef](#)]
22. Kryukov, A.; Blagoeva, D.; Debarberis, L. Flux Effect Analysis in WWER-440 Reactor Pressure Vessel Steels. *J. Nucl. Mater.* **2013**, *443*, 171–175. [[CrossRef](#)]
23. Wagner, A.; Bergner, F.; Chaouadi, R.; Hein, H.; Hernández-Mayoral, M.; Serrano, M.; Ulbricht, A.; Altstadt, E. Effect of Neutron Flux on the Characteristics of Irradiation-Induced Nanofeatures and Hardening in Pressure Vessel Steels. *Acta Mater.* **2016**, *104*, 131–142. [[CrossRef](#)]
24. Toyama, T.; Yamamoto, T.; Ebisawa, N.; Inoue, K.; Nagai, Y.; Odette, G.R. Effects of Neutron Flux on Irradiation-Induced Hardening and Defects in RPV Steels Studied by Positron Annihilation Spectroscopy. *J. Nucl. Mater.* **2020**, *532*, 152041. [[CrossRef](#)]
25. Kuleshova, E.A.; Zhuchkov, G.M.; Fedotova, S.V.; Maltsev, D.A.; Frolov, A.S.; Fedotov, I.V. Precipitation Kinetics of Radiation-Induced Ni-Mn-Si Phases in VVER-1000 Reactor Pressure Vessel Steels under Low and High Flux Irradiation. *J. Nucl. Mater.* **2021**, *553*, 153091. [[CrossRef](#)]
26. Altstadt, E.; Keim, E.; Hein, H.; Serrano, M.; Bergner, F.; Viehrig, H.-W.; Ballesteros, A.; Chaouadi, R.; Wilford, K. FP7 Project LONGLIFE: Overview of Results and Implications. *Nucl. Eng. Des.* **2014**, *278*, 753–757. [[CrossRef](#)]
27. Hyde, J.M.; DaCosta, G.; Hatzoglou, C.; Weekes, H.; Radiguet, B.; Styman, P.D.; Vurpillot, F.; Pareige, C.; Etienne, A.; Bonny, G.; et al. Analysis of Radiation Damage in Light Water Reactors: Comparison of Cluster Analysis Methods for the Analysis of Atom Probe Data. *Microsc. Microanal.* **2017**, *23*, 366–375. [[CrossRef](#)]
28. Selim, F.A.; Wells, D.P.; Harmon, J.F.; Kwofie, J.; Spaulding, R.; Erickson, G.; Roney, T. Bremsstrahlung-Induced Highly Penetrating Probes for Nondestructive Assay and Defect Analysis. *Nucl. Instrum. Methods Phys. Res. Sect. Accel. Spectrometers Detect. Assoc. Equip.* **2002**, *495*, 154–160. [[CrossRef](#)]
29. Butterling, M.; Anwand, W.; Cowan, T.E.; Hartmann, A.; Jungmann, M.; Krause-Rehberg, R.; Krille, A.; Wagner, A. Gamma-Induced Positron Spectroscopy (GiPS) at a Superconducting Electron Linear Accelerator. *Nucl. Instrum. Methods Phys. Res. Sect. B Beam Interact. Mater. At.* **2011**, *269*, 2623–2629. [[CrossRef](#)]
30. Wagner, A.; Butterling, M.; Liedke, M.O.; Potzger, K.; Krause-Rehberg, R. *Positron Annihilation Lifetime and Doppler Broadening Spectroscopy at the ELBE Facility*; AIP Conference Proceedings 1970: Newport News, VA, USA, 2018; p. 040003. [[CrossRef](#)]
31. Kirkegaard, P. *PALSFIT: A Computer Program for Analysing Positron Lifetime Spectra*; Risø National Laboratory for Sustainable Energy: Roskilde, Denmark, 2009; ISBN 978-87-550-3691-8.
32. Keiderling, U. The New “BerSANS-PC” Software for Reduction and Treatment of Small Angle Neutron Scattering Data. *Appl. Phys. Mater. Sci. Process.* **2002**, *74*, s1455–s1457. [[CrossRef](#)]
33. Martelli, S.; Di Nunzio, P.E. Particle Size Distribution of Nanospheres by Monte Carlo Fitting of Small Angle X-Ray Scattering Curves. *Part. Part. Syst. Charact.* **2002**, *19*, 247–255. [[CrossRef](#)]
34. Hernández-Mayoral, M.; Heintze, C.; Oñorbe, E. Transmission Electron Microscopy Investigation of the Microstructure of Fe–Cr Alloys Induced by Neutron and Ion Irradiation at 300 °C. *J. Nucl. Mater.* **2016**, *474*, 88–98. [[CrossRef](#)]
35. Kuriplach, J.; Melikhova, O.; Domain, C.; Becquart, C.S.; Kulikov, D.; Malerba, L.; Hou, M.; Almazouzi, A.; Duque, C.A.; Morales, A.L. Vacancy-Solute Complexes and Their Clusters in Iron. *Appl. Surf. Sci.* **2006**, *252*, 3303–3308. [[CrossRef](#)]

36. Nagai, Y.; Tang, Z.; Hasegawa, M.; Kanai, T.; Saneyasu, M. Irradiation-Induced Cu Aggregations in Fe: An Origin of Embrittlement of Reactor Pressure Vessel Steels. *Phys. Rev. B* **2001**, *63*, 134110. [[CrossRef](#)]
37. Wagner, A.; Anwand, W.; Butterling, M.; Cowan, T.E.; Fiedler, F.; Fritz, F.; Kempe, M.; Krause-Rehberg, R. Positron-Annihilation Lifetime Spectroscopy Using Electron Bremsstrahlung. *J. Phys. Conf. Ser.* **2015**, *618*, 012042. [[CrossRef](#)]
38. Soisson, F.; Barbu, A.; Martin, G. Monte Carlo Simulations of Copper Precipitation in Dilute Iron-Copper Alloys during Thermal Ageing and under Electron Irradiation. *Acta Mater.* **1996**, *44*, 3789–3800. [[CrossRef](#)]
39. Odette, G.R.; Yamamoto, T.; Williams, T.J.; Nanstad, R.K.; English, C.A. On the History and Status of Reactor Pressure Vessel Steel Ductile to Brittle Transition Temperature Shift Prediction Models. *J. Nucl. Mater.* **2019**, *526*, 151863. [[CrossRef](#)]
40. Bergner, F.; Ulbricht, A.; Wagner, A. Long-Term Aging Effects in RPV Steel, Scientific Report HZDR-056. 2014. Available online: <https://www.hzdr.de/Publications/Publ-21162> (accessed on 19 January 2022).
41. Christien, F.; Barbu, A. Modelling of Copper Precipitation in Iron during Thermal Aging and Irradiation. *J. Nucl. Mater.* **2004**, *324*, 90–96. [[CrossRef](#)]
42. Mansur, L.K. Void Swelling in Metals and Alloys Under Irradiation: An Assessment of the Theory. *Nucl. Technol.* **1978**, *40*, 5–34. [[CrossRef](#)]
43. Seeger, A.K. On the Theory of Radiation Damage and Radiation Hardening. In Proceedings of the Second United Nations International Conference on The Peaceful Uses of Atomic Energy, Geneva, Switzerland, 1–13 September 1958; 1958; Volume 6, pp. 250–273.
44. Wagner, A.; Ulbricht, A.; Bergner, F.; Altstadt, E. Influence of the Copper Impurity Level on the Irradiation Response of Reactor Pressure Vessel Steels Investigated by SANS. *Nucl. Instrum. Methods Phys. Res. Sect. B-Beam Interact. Mater. At.* **2012**, *280*, 98–102. [[CrossRef](#)]
45. Tabor, T. *The Hardness of Metals*; Clarendon Press: Oxford, UK, 1948.